

Modeling Pixel-Level Electrical Crosstalk for the Athena X-IFU

Bachelorarbeit aus der Physik

Vorgelegt von
Christian Thomas Kirsch
30. September 2016

Dr. Karl Remeis-Sternwarte Bamberg
Friedrich-Alexander-Universität Erlangen-Nürnberg



Betreuer: Prof. Dr. Jörn Wilms

Abstract

As part of the end-to-end simulation software for the Athena X-IFU instrument, I have developed a pixel-level crosstalk simulator for transition-edge sensors (TES) in frequency domain multiplexing (FDM).

After deriving the electrical crosstalk effects appearing due to FDM and describing their implementation, I present simulation results concerning the effect of crosstalk on a TES pixel. I find both a constant operating point offset, as well as weak, additional pulses transferred to a signal pixel. After performing an energy reconstruction for pure crosstalk events as well as for photon events influenced by crosstalk, I provide energy and time dependence lookup tables for use in the SIXTE tool `xi fupipeline`. Based on these results, I discuss further refinements to be made in the current crosstalk implementation.

Contents

1	Introduction	3
2	tessim Simulations	6
3	Crosstalk in FDM	8
3.1	FDM Circuit	8
3.2	Carrier Overlap	9
3.3	Common Impedance	10
3.4	Additional Crosstalk Effects	11
4	Implementation in teslute	12
5	Results	13
5.1	Operating Point Offset	13
5.2	Crosstalk Pulses	14
5.3	Lookup Table	16
5.4	Time Dependence	19
6	Outlook and Conclusions	23
7	Acknowledgments	23
	List of Figures	24
	List of Tables	24
	References	24

1 Introduction

The Athena mission (Nandra et al., 2013) is an X-ray observatory approved by ESA as the second of the large-class missions in their Cosmic Vision Programme. It addresses the theme of “The Hot and Energetic Universe”. Its launch is currently planned for January 2029; as such, its two instruments – the X-ray Integral Field Unit (X-IFU) and the Wide Field Imager (WFI) – are currently in active development. The focus of this Bachelor’s thesis lies on the simulation of the X-IFU.

The X-IFU (Barret et al., 2016) is an array of transition-edge sensors (TES). Its general purpose is to perform imaging spectroscopy at a resolution of 2.5 eV for photons below 7 keV, while fulfilling the field of view requirement of $5'$ at a resolution of $5''$. Such spatially resolved spectroscopy can be used, for instance, to reconstruct the bulk motion of gases in galaxy clusters or to resolve the iron K complex at 6.4 keV, as shown by Hitomi Collaboration et al. (2016) for the Perseus cluster.

Transition-edge sensors are an application of the superconducting phase transition first discovered by Andrews et al. (1942). See Irwin & Hilton (2005) for a review. For the X-IFU, they will be used as thermal equilibrium calorimeters (Andrews et al., 1949; McCammon, 2005) by measuring the thermal energy deposited by an absorbed photon via a change in resistance, as a kind of resistive thermometer. Their differences to ordinary resistive thermometers are their steep $R(T)$ -curves, as well as the fact that they are designed to measure changes in temperature at a very short time scale.

Their working principle is as follows: A TES is a superconductor which is operated at its transition temperature. As such, its resistance is somewhere between its normal conductor resistance and a resistance of $\approx 0\Omega$. See Figure 1 for an example $R(T)$ -curve. In order to remain at their operating point, the TES sensors are connected to a low temperature heat bath, which cools the TES down and compensates for the Joule heating caused by the current flowing through the detector when it is at its operating point.

Close to the transition temperature, even the fairly small amount of heat dumped by a photon is strong enough to change the TES resistance by an order of magnitude. If a TES is operated at a constant bias voltage, this will lead to a drop in the current flowing to the TES. This change in the TES current is then measured as output.

In order for a TES to return to its operating point within a short time, one takes advantage of so-called negative electrothermal feedback – since the Joule power of a resistor is proportional to $V \cdot I$, the drop in current due to the increased TES resistance leads to a proportional drop in the Joule heating of the TES. Effectively, the TES receives additional cooling, bringing it back to its equilibrium state.

For the regime within which the TES resistance is linear in temperature (see Section 2), the differential equations describing a TES have been solved for a delta-function energy pulse (Irwin & Hilton, 2005), which is a first order approximation for photon absorption. The results of these equations are pulses in the TES current with characteristic rise- and fall-times.

The shapes and amplitudes of these current pulses are then dependent on the energy of the incident photon (see Fig 3). Consequently, the energy of an incident photon can be retrieved by analyzing exactly those current pulses. For this, a variety of reconstruction algorithms are currently being tested in the framework of the X-IFU project (see Peille et al. (2016) for a summary).

The above descriptions indicate that the measurement capabilities of the X-IFU are extremely dependent on device parameters such as the rise- and fall-times of the TES-Sensors (time resolution), their heat capacity (which determines the change in temperature for a given photon energy), the geometric design of the TES array (spatial resolution) as well as the energy reconstruction method. Due to the many interacting factors involved, it is very helpful to develop a simulator for the entire telescope – this way, one can easily change system parameters in a simulation instead of experimentally comparing many parameter combinations, saving development costs. This is especially important for X-ray observatories, which have to be planned very carefully before being sent into space.

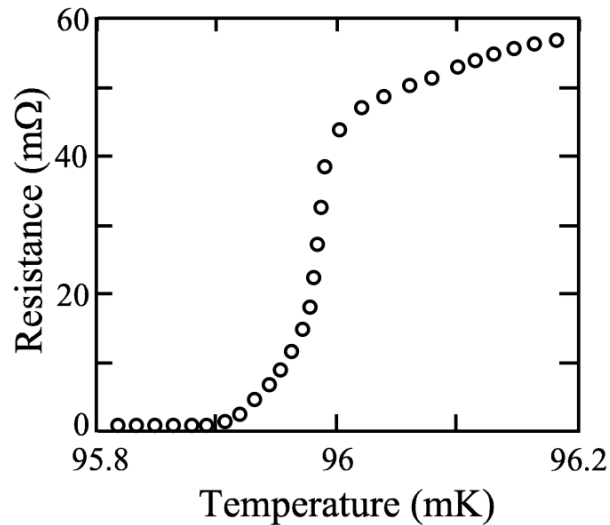


Figure 1: Figure and caption taken from Irwin & Hilton (2005): “The transition of a superconducting film (a Mo/Cu proximity bilayer) from the normal to the superconducting state near 96 mK. The sharp phase transition suggests its use as a sensitive thermometer.”

The end-to-end simulator for the X-IFU is being developed as part of the SIXTE (Simulation of X-ray Telescopes) software package (Wilms et al., 2014). This package is open software (available at <http://www.sternwarte.uni-erlangen.de/sixte>) and designed to be as modular as possible – by combining different software tools, one can essentially build an instrument from scratch using implemented routines, starting with the generation of photons from defined sources, simulating the photon imaging process and detector response and ending with the subsequent energy readout.

SIXTE contains two tools for the simulation of transition-edge sensors: `tessim` (Wilms et al., 2016) and the `xifupipeline`. Their simulation concept is outlined in Fig. 2. The purpose of `tessim` is to accurately simulate the physics of a single TES pixel using the differential equations from Irwin & Hilton (2005). However, running these simulations for an entire array of TES pixels would require a prohibitive amount of computation time. For detector-level simulations, one instead uses the `xifupipeline`: It calculates the detector response via interpolating from tables created via `tessim` or retrieved from experimental data. This approach, while less accurate, requires much less computational effort, allowing the simulation of observations at or below real time.

To predict the energy resolution of the X-IFU, `tessim` already implements the known noise-effects of transition-edge sensors (Kinnunen, 2011). However, there is one effect degrading the resolution which has not been implemented yet – that of crosstalk.

Crosstalk is a general term for the unintended transmission of information between signal channels – for TES arrays, this would mean that a signal in a perturbing TES would have an effect on the readout of another TES. Among the various types of crosstalk, this thesis focuses on electrical crosstalk. This type of crosstalk is caused by multiplexing, which is the combination of the signals of multiple pixels into one channel. The need for this procedure comes from a limited cooling power for the instrument – since any wiring from the room temperature readout electronics to the sub-Kelvin detector pixels is a thermal link, all available cooling power would be wasted in the heat differential if one directly connected each individual pixel to the readout electronics.

The goal of this Bachelor’s thesis is the implementation of crosstalk in the `tessim` simulator. To that extent, I will first describe the simulations done by `tessim` in more detail (Section 2). Then, I will outline the planned multiplexing scheme for the X-IFU and derive the electrical crosstalk resulting from this method (Section 3). The implementation of these effects in `tessim` – or rather, a new tool

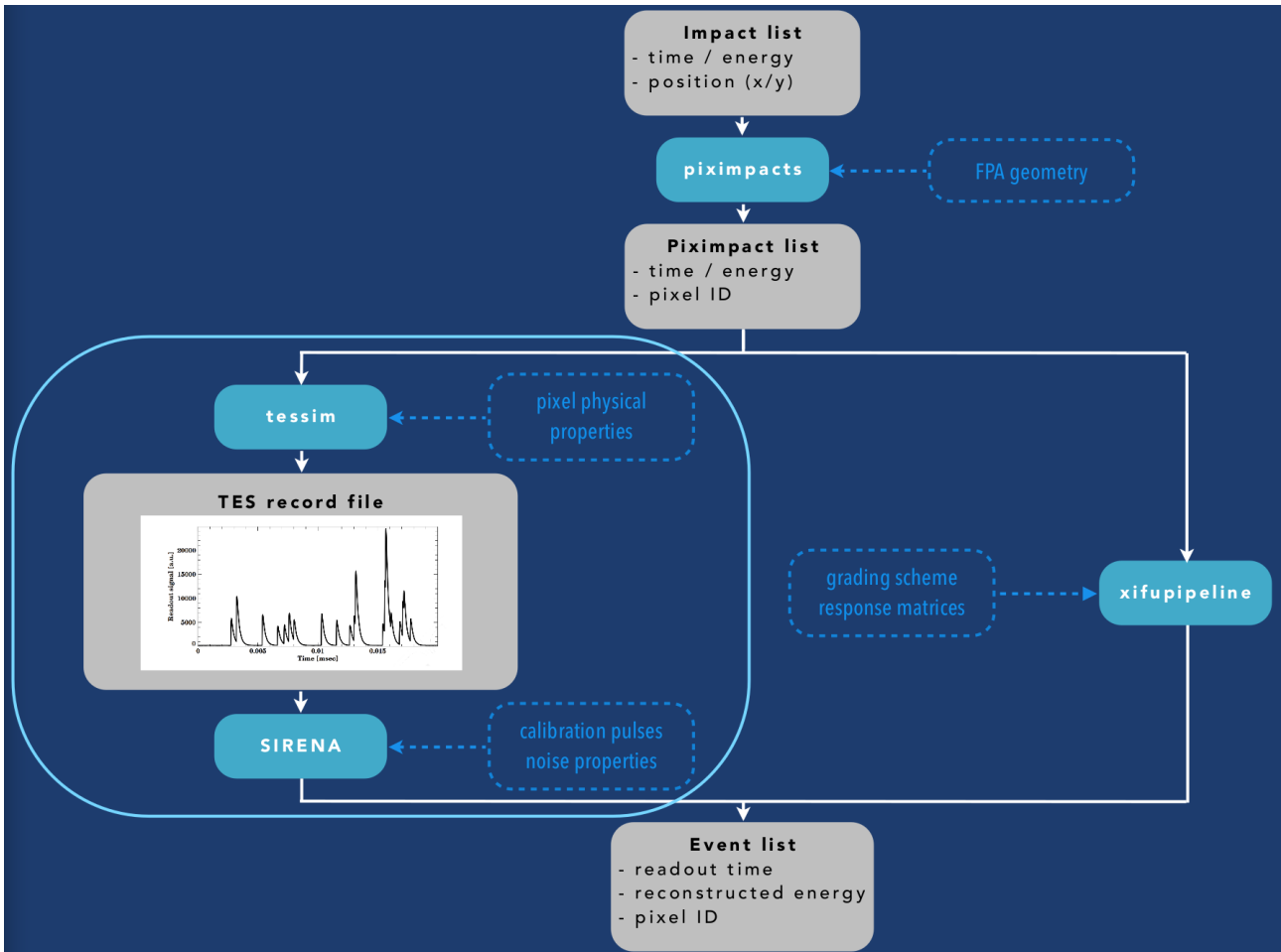


Figure 2: Simulation principle of `tessim` and the `xifupipeline`. Energy events from a list containing photon arrival times and energies can either be calculated via `tessim` with an additional energy reconstruction scheme (here `SIRENA`), or interpolated from existing tables via the `xifupipeline`. Figure provided by Philippe Peille (priv. comm.).

based on it, called `teslute` – will be shown in Section 4. Following the implementation, I will apply `teslute` and show the results of various simulations providing data for use in the `xifupipeline` (Section 5), after which I will conclude and provide an outlook of possible future modifications to both `tessim` and `teslute`.

2 tessim Simulations

`tessim` (Wilms et al., 2016) is the current transition-edge sensor simulator tool implemented in SIXTE (Wilms et al., 2014). Based on an input FITS file describing photon arrival times and energies for the simulated pixel, it solves the differential equations for TES temperature T and current I (Irwin & Hilton, 2005)

$$C \frac{dT}{dt} = -P_b + R(T, I)I^2 + P + \text{Noise} \quad (1)$$

$$L \frac{dI}{dt} = V - IR_L - IR(T, I) + \text{Noise}, \quad (2)$$

where C is the heat capacity of the TES and its absorber, P_b is the power flowing from the TES to the heat bath, P is the signal power due to an incident photon and $R(T, I)I^2$ is the Joule power deposited in the TES ($R(T, I)$ being its resistance). In the current equation, L is the inductance – which may be an effective inductance, see Section 3 – V is the bias voltage and R_L is the load resistance. For an example TES circuit, see Figure 4.

The modeled noise sources include thermal fluctuations in the heat conduction between the TES and the heat bath, Johnson noise in the load resistor and amplifier noise during readout. The Johnson noise in the TES is calculated via a nonlinear equilibrium ansatz (NLEA, see Irwin & Hilton (2005)), which takes into account the nonzero current dependence β of $R(T, I)$. The TES noise also includes an unexplained excess noise found in experiments (Kinnunen, 2011), quantified by an empirical parameter m .

Currently, `tessim` uses a Runge-Kutta differential equation solver at a fixed step size. For future developments, it is planned to use an adaptive step size statistical differential equation solver to properly handle the inherently statistical heat conduction behavior at such low temperatures.

For $R(T, I)$, `tessim` uses a resistance model linear in both temperature and current around the operating point resistance R_0 , current I_0 and temperature T_0

$$R(T, I) = R_0 + \left. \frac{\partial R}{\partial T} \right|_{I_0} (T - T_0) + \left. \frac{\partial R}{\partial I} \right|_{T_0} (I - I_0), \quad (3)$$

where we encode the partial derivatives via the two parameters

$$\alpha = \left. \frac{\partial \log R}{\partial \log T} \right|_{I_0} = \frac{T_0}{R_0} \left. \frac{\partial R}{\partial T} \right|_{I_0} \quad (4)$$

$$\beta = \left. \frac{\partial \log R}{\partial \log I} \right|_{T_0} = \frac{I_0}{R_0} \left. \frac{\partial R}{\partial I} \right|_{T_0}. \quad (5)$$

This ansatz is predicated on the assumption that one remains close to the operating point of the TES, which may not be the case for high count rate scenarios. More complex resistor models such as those discussed by Wang et al. (2012) will be implemented in the future.

The output of `tessim` is a FITS file containing the current, $I(t)$. Optionally, it may either return a continuous current stream throughout the entire simulation or return triggered records. Records have a fixed length in samples – their actual duration in seconds depends on the sample rate – with the idea being that in an actual spacecraft, not the entire data stream of measured currents is used to calculate the energy of incident photons, as this would waste computational resources. Rather, the data stream goes through a so called trigger, which, using various means (Wilms et al., 2016), detects events in the data stream and forwards them to the reconstruction algorithm. A trigger may be implemented, for example, by thresholding on a moving average of recently recorded samples – triggering when that moving average surpasses a set value – or thresholding on a low-pass filtered derivative of the current stream.

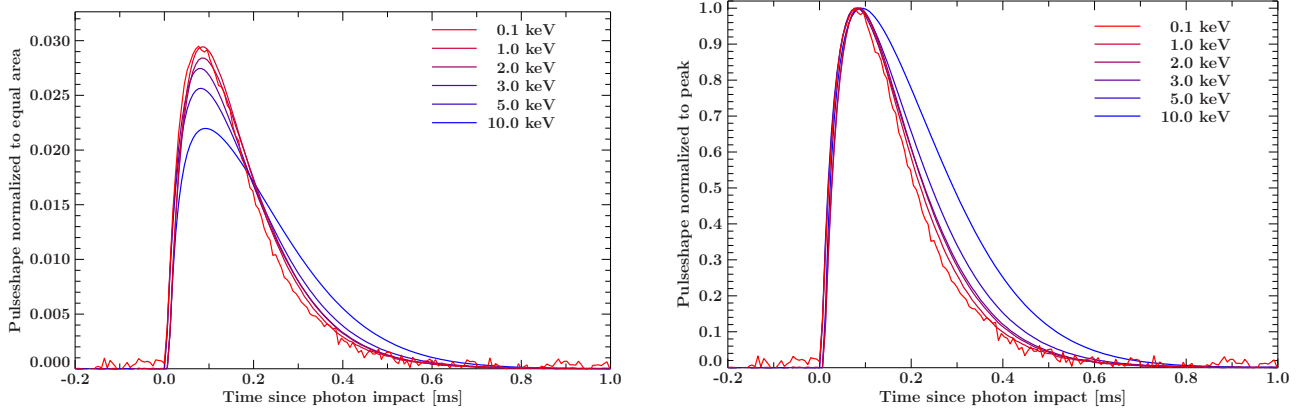


Figure 3: An example of current pulses produced by `tessim` for varying photon energies. *Left*: Pulses normalized to the same area. *Right*: Pulses normalized to the same peak current. Figure taken from Wilms et al. (2016).

Figure 3 shows part of a data stream generated via `tessim`. Note that the current output is always given as $I_{\text{start}} - I(t)$, i.e. only as the difference from the equilibrium current of the TES, with an inverted sign.

Using the output produced by `tessim`, several energy reconstruction methods are currently being developed for the X-IFU (Peille et al., 2016). In Section 5, I will use optimal filtering (Rey, 1991) to reconstruct the energies of both pure crosstalk pulses as well as the energies of pulses affected by crosstalk. We will see there that the impact of crosstalk is also dependent on the applied energy reconstruction method.

In order to provide an output which the reconstruction methods will have to work with in the actual X-IFU, `tessim` provides the output current both in Amperes, as a double-precision float, as well as in artificially digitized Analog Digital Units. All reconstruction methods use the latter output, which simulates the instrument's ADC, providing the current transformed into unsigned 16-bit integers.

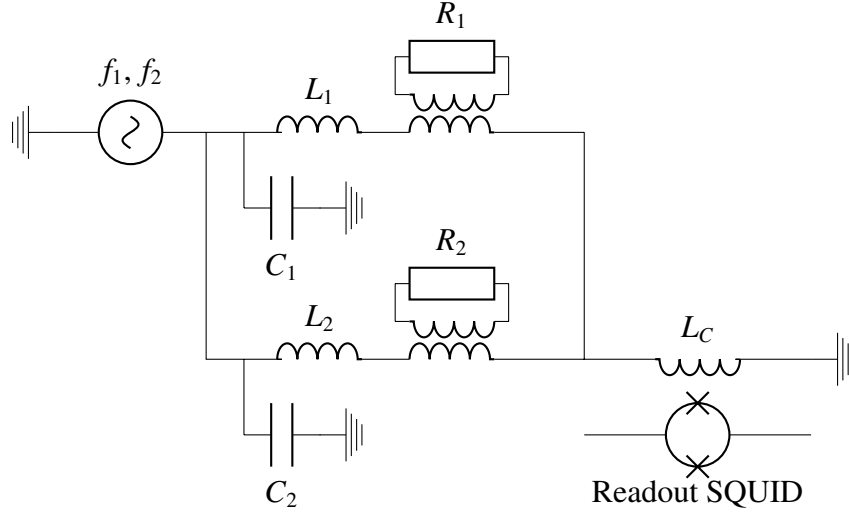


Figure 4: Circuit diagram for the FDM-readout scheme.

3 Crosstalk in FDM

3.1 FDM Circuit

Frequency domain multiplexing is a technique for combining the current output of multiple TES pixels into one signal from which all necessary data can be retrieved afterwards. For an outline of the proposed X-IFU readout scheme, refer to den Hartog et al. (2014). See Figure 4 for a schematic of the readout circuit with two TES-pixels.

A voltage source provides sinusoidal carrier voltages at frequencies $f_1, f_2 \dots$. These bias voltages are applied to each TES (denoted by R_i) in parallel. Every parallel circuit contains a capacitor C_i and an inductor L_i chosen such that $\frac{1}{\sqrt{L_i C_i}} = 2\pi f_i = \omega_i$, so ideally, each TES R_i only couples to the bias voltage at frequency f_i . Each TES is coupled to the LC-circuit via a transformer coupling with a Transformer Turns Ratio a , where the TES-subcircuit is considered to be the primary circuit.

The total current through these parallel LRC-circuits is simply the sum of currents through each circuit individually. This current then flows through the readout-coil (inductance L_C) which is magnetically coupled to a SQUID. After additional amplification, these currents are demodulated, such that the current through each TES separately can be retrieved and further analyzed.

This circuit can be further simplified by replacing the transformer coupling with equivalent values by assuming ideal transformers; either by up-transforming the TES resistances by a factor of a^2 – thus looking at the LC-circuit, where crosstalk arises – or by down-transforming all inductances by a factor of $\frac{1}{a^2}$, up-transforming the capacitances by a^2 and multiplying all currents and voltages in the LC-circuit by a or $\frac{1}{a}$, respectively. The latter transformation assumes that both TES resistors are coupled with the same transformer turns ratio and represents the TES-circuit. Since tessim simulates the TES-circuit, I will use latter transformation.

After using this transformation, one can further simplify the readout circuit by connecting all grounds – see Figure 5. The SQUID – which is still inductively coupled to L_C – has been omitted. In this case, the current $I_1 + I_2$ reaches the readout coil, L_C .

Using this FDM-Circuit, we can now examine the resulting electrical crosstalk. We define R_1 to be the pixel whose current we are interested in reading out (the "Signal TES") and R_2 to be the pixel which produces crosstalk (the "Perturber TES").

The following calculations expand on Dobbs et al. (2012), although their calculations assume the same

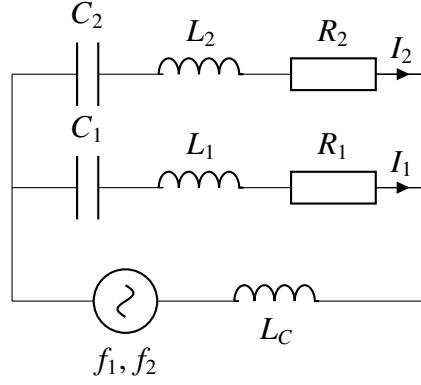


Figure 5: Simplified circuit diagram corresponding to Fig. 4. The SQUID has been omitted.

inductance L for all filter coils – only the capacitances differ between filters. They also use different notation and interpret their results for bolometers – which measure a change in a power flow, unlike calorimeters, which measure particle energies.

3.2 Carrier Overlap

Since we are considering a readout circuit with two TES pixels, we will separately look at the currents produced at their carrier frequencies. These equations are thus not solved in the time domain, like they are for the individual pixels in `tessim`. The differential equation solver provides values for R_1 , R_2 and $I_1^{\omega_1}$ as well as $I_2^{\omega_2}$, which are the currents through pixels 1 and 2 at their respective carrier frequencies. At the carrier frequency ω_1 , we can use Kirchoff's circuit laws to obtain two equations describing the currents in this circuit,

$$V_b^{\omega_1} = i\omega_1 L_C (I_1^{\omega_1} + I_2^{\omega_1}) + \left(R_1 + i\omega_1 L_1 + \frac{1}{i\omega_1 C_1} \right) I_1^{\omega_1} = i\omega_1 L_C (I_1^{\omega_1} + I_2^{\omega_1}) + R_1 I_1^{\omega_1} \quad (6)$$

$$V_b^{\omega_1} = i\omega_1 L_C (I_1^{\omega_1} + I_2^{\omega_1}) + \left(R_2 + i\omega_1 L_2 + \frac{1}{i\omega_1 C_2} \right) I_2^{\omega_1}, \quad (7)$$

where the term $i\omega_1 L_1 + \frac{1}{i\omega_1 C_1}$ cancels, since $\omega_i = \frac{1}{\sqrt{L_i C_i}}$.

Solving Eq. 7 for $I_2^{\omega_1}$, we obtain

$$I_2^{\omega_1} = \frac{V_b^{\omega_1} - i\omega_1 L_C I_1^{\omega_1}}{R_2 + i\omega_1(L_2 + L_C) + \frac{1}{i\omega_1 C_2}} = \frac{V_b^{\omega_1} - i\omega_1 L_C I_1^{\omega_1}}{R_2 + iZ_{I,\omega_1}}, \quad (8)$$

where

$$Z_{I,\omega_1} = \omega_1 (L_2 + L_C) - \frac{1}{\omega_1 C_2} = \omega_1 (L_2 + L_C) - \frac{\omega_2^2 L_2}{\omega_1} \quad (9)$$

$$= L_2 \frac{\omega_1^2 - \omega_2^2}{\omega_1} + \omega_1 L_C. \quad (10)$$

Following this, we can separate $I_2^{\omega_1}$ into its real and imaginary components, yielding

$$I_2^{\omega_1} = \frac{\left[V_b^{\omega_1} R_2 - \omega_1 Z_{I,\omega_1} L_C I_1^{\omega_1} \right] - i \left[V_b^{\omega_1} Z_{I,\omega_1} + \omega_1 R_2 L_C I_1^{\omega_1} \right]}{R_2^2 + Z_{I,\omega_1}^2}. \quad (11)$$

This crosstalk current is generally known as carrier overlap – at the frequency ω_1 , the pixel 2 emits an additional current, which is read out "on top" of the actual signal current $I_1^{\omega_1}$. Its signal depends very much on the readout mode – assuming $I_1^{\omega_1}$ is in phase with $V_b^{\omega_1}$, one can use IQ-demodulation to separate the readout current into the part in phase with the bias voltage and the part phase shifted by 90° , called the I and Q mode, respectively. In the readout, the I-current would be $I_1^{\omega_1} + \Re(I_2^{\omega_1})$ and the Q-current would be $\Im(I_2^{\omega_1})$.

One can also simply consider the amplitude of the output current, regardless of phase. In this case, the measured current along with crosstalk would be

$$I_{\text{readout}} = \sqrt{\left(I_1^{\omega_1} + \Re(I_2^{\omega_1})\right)^2 + \left(\Im(I_2^{\omega_1})\right)^2}, \quad (12)$$

where $I_1^{\omega_1}$ is assumed to be entirely real.

Dobbs et al. (2012) also give an estimation for the magnitude of this crosstalk: By neglecting the L_C -contribution and assuming that $\omega_1 \approx \omega_2$, one can estimate $Z_{I,\omega_1} \approx 2L_2(\omega_1 - \omega_2)$. Using a Taylor expansion, one can approximate the ratio between the magnitudes of the current pulses for both pixels as

$$\left|\frac{\Delta I_2^{\omega_1}}{\Delta I_1^{\omega_1}}\right| \approx \left(\frac{R_2}{2L_2(\omega_1 - \omega_2)}\right)^2. \quad (13)$$

While my simulations are more accurate than this estimation – especially with regards to Z_{I,ω_1} at higher frequency distances – it is still useful as an order-of-magnitude estimation of crosstalk pulses.

3.3 Common Impedance

At the carrier frequency ω_2 , we can retrieve a similar set of equations describing the readout circuit,

$$V_b^{\omega_2} = i\omega_2 L_C (I_1^{\omega_2} + I_2^{\omega_2}) + \left(R_1 + i\omega_2 L_1 + \frac{1}{i\omega_2 C_1}\right) I_1^{\omega_2} \quad (14)$$

$$V_b^{\omega_2} = i\omega_2 L_C (I_1^{\omega_2} + I_2^{\omega_2}) + \left(R_2 + i\omega_2 L_2 + \frac{1}{i\omega_2 C_2}\right) I_2^{\omega_2} = i\omega_2 L_C (I_1^{\omega_2} + I_2^{\omega_2}) + R_2 I_2^{\omega_2}, \quad (15)$$

where now the terms with L_2 and C_2 cancel, $I_2^{\omega_2}$ is the on-resonance current and $I_1^{\omega_2}$ is the crosstalk, which we can calculate as before by rewriting Eq. 14

$$I_1^{\omega_2} = \frac{\left[V_b^{\omega_2} R_1 - \omega_2 Z_{I,\omega_2} L_C I_2^{\omega_2}\right] - i \left[V_b^{\omega_2} Z_{I,\omega_2} + \omega_2 R_1 L_C I_2^{\omega_2}\right]}{R_1^2 + Z_{I,\omega_2}^2}, \quad (16)$$

where

$$Z_{I,\omega_2} = \omega_2(L_1 + L_C) - \frac{1}{\omega_2 C_1} = \omega_2(L_1 + L_C) - \frac{\omega_1^2 L_1}{\omega_2} \quad (17)$$

$$= L_1 \frac{\omega_2^2 - \omega_1^2}{\omega_2} + \omega_2 L_C. \quad (18)$$

This current is just the carrier overlap crosstalk produced by the pixel 1 at the frequency ω_2 . However, we are not interested in the readout of the pixel 2. Instead, we consider the effect of this current on the pixel 1, as it causes an additional Joule heating

$$P(t) = \Re \left(V_b^{\omega_2}(t) I_1^{\omega_2}(t) \right) = V_b^{\omega_2} \Re \left(I_1^{\omega_2} \right) \sin^2(\omega_2 t) \quad (19)$$

$$= \frac{\left(V_b^{\omega_2}\right)^2 R_1 - V_b^{\omega_2} \omega_2 Z_{I,\omega_2} L_C I_2^{\omega_2}}{R_1^2 + Z_{I,\omega_2}^2} \sin^2(\omega_2 t). \quad (20)$$

By integrating over one cycle of the carrier voltage and dividing by $T = 2\pi/\omega_2$, we obtain the average power deposited in the pixel 1 due to common impedance crosstalk as

$$P_{\text{common}} = \frac{1}{2} \cdot \frac{(V_b^{\omega_2})^2 R_1 - V_b^{\omega_2} \omega_2 Z_{I,\omega_2} L_C I_2^{\omega_2}}{R_1^2 + Z_{I,\omega_2}^2}. \quad (21)$$

It is interesting to look at the change in the common impedance crosstalk when the current $I_2^{\omega_2}$ changes by dI , as is the case when a photon is absorbed by the perturber pixel;

$$dP_{\text{common}} = -\frac{dI}{2} \cdot \frac{V_b^{\omega_2} \omega_2 Z_{I,\omega_2} L_C}{R_1^2 + Z_{I,\omega_2}^2}. \quad (22)$$

If we neglect R_1 in this equation and recall that the sign of Z_{I,ω_2} equals the sign of $\omega_2 - \omega_1$ (neglecting the effect of L_C on Z_{I,ω_2} , which is usually very small), we see that this type of crosstalk can cause either negative or positive Joule heating, depending on the choice of perturber and signal frequency. Note that usually, the sign of dI is also negative, since the photon arriving in the perturber pixel raises its resistance, thus lowering $I_2^{\omega_2}$ under constant voltage bias.

Altogether, this means that the common impedance crosstalk effect has the same sign – in the sense of deposited energy – as $\omega_2 - \omega_1$.

For a rough estimation of this crosstalk, one can – similarly to the case of carrier overlap crosstalk – write $Z_{I,\omega_2} \approx 2L_1(\omega_2 - \omega_1)$. Note that L_C is usually much smaller than L_1 . Neglecting the contribution of R_1 in the denominator of Eq. 22, one finds

$$dP_{\text{common}} \approx -\frac{dI V_b^{\omega_2}}{2} \frac{\omega_2 L_C}{2L_1(\omega_2 - \omega_1)}. \quad (23)$$

Note that the term $(dI V_b^{\omega_2}/2)$ equals the negative electrothermal feedback resetting the pixel 2 to its operating point.

3.4 Additional Crosstalk Effects

For the sake of completeness, I will summarize some known crosstalk effects which have not been implemented in my own simulations. Refer to den Hartog et al. (2016) for the effect of these types of crosstalk on observations as well as some mitigation options.

The first mechanism, which is already implemented in the `xifupipeline`, is referred to as thermal crosstalk. It is the result of thermal coupling between two physically adjacent pixels, where thermal power flows from a pixel which has been heated by an incident photon to other pixels or the array itself. Iyomoto et al. (2008) have measured this crosstalk for an 8x8-pixel array. The magnitude of this crosstalk is dependent on the layout and construction of the actual array. The `xifupipeline` uses experimental estimations in order to incorporate this effect.

Dobbs et al. (2012) describe a crosstalk due to inductor cross-coupling: This crosstalk is electrical in nature and comes from the fact that the filter inductors of physically adjacent pixels couple magnetically. This leads to current modulations in any particular channel being transferred to adjacent pixels. By making sure that neighbouring inductors are far apart in frequency space as well as by installing magnetic shielding between filter inductors, this crosstalk can be mitigated.

A more complex crosstalk effect arises from the non-linear amplification of the readout SQUID, described by den Hartog et al. (2016). For each frequency channel, the SQUID output also contains higher harmonics of that channel. These higher harmonics may affect the readout of other channels, where the precise effect once again depends on the frequency spacing as well as the difference in arrival times of these photons. It is implemented in the `xifupipeline` via a lookup-table dependent on the arrival times of two particular photons.

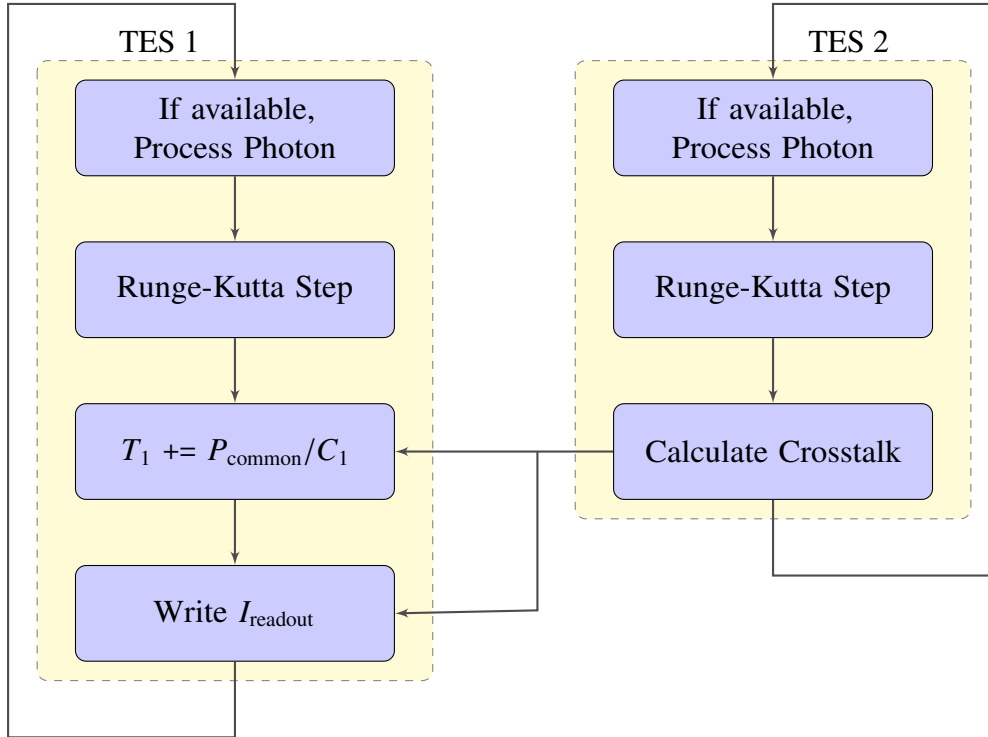


Figure 6: Working principle of teslute.

4 Implementation in teslute

In order to produce a first estimate of the impact of crosstalk, I wrote a new SIXTE tool called `teslute` (Transition-Edge Sensor LookUp-Table gENERator). It is based on `tessim` and will be merged into `tessim` in the future. As the name suggests, its first purpose was to generate so-called lookup tables – to be further outlined in Section 5.3 – which will be used in the `xifupipeline`.

The general principle of `teslute` is outlined in Figure 6. Essentially, I use the differential equation solver of `tessim` to simulate the signal and perturber pixel (1 and 2) separately, calculating the crosstalk emitted by the perturber pixel after each differential equation step.

The common impedance crosstalk is calculated via Eq. 21; the temperature of the signal TES is then simply changed by the calculated Joule power divided by its heat capacity.

For the carrier overlap, there are several options: By default, the usual readout current is simply replaced by the current calculated in Eq. 12. Optionally, it is also possible to switch the readout of the signal TES to either the I or Q channel, where the crosstalk is applied accordingly.

In order to later analyze crosstalk pulses which are too small to be digitized or simply below the triggering threshold, I have also implemented an idealized triggering scheme based on the actual impact times read from the pixel impact file. Thus, this trigger actually knows the exact arrival times of each photon, disregarding any change in the actual TES. This trigger will, naturally, only be used for simulation tests and debugging.

While one could also construct a new system of differential equations encompassing the entire readout circuit in order to solve the entire system as one set of coupled equations, I have chosen this rather modular approach. The purpose behind this choice is an easy extensibility – I could very easily add any amount of additional TES pixels emitting crosstalk to pixel 1, simulating the crosstalk effects of a larger readout-circuit. By simulating all pixels separately, we also have the option of running them at different integration step sizes after implementing an adaptive equation solver. Describing the entire

Table 1: Physical parameters of the TES-pixels simulated in this thesis.

Parameter	Value
Pixel Type	SPA Hybrid
Sample Frequency	156.250 kHz
Sample Time	6.4 μ s
I_0	72.6672 μ A
R_0	1.1 m Ω
L_{filter}	2 μ H
L_C	2 nH
TTR	4.052
α	100
β	10
T_0	90 mK
T_{bath}	55 mK
C_{Absorber}	0.26 pJ/K
G	300 pW/K

system via one set of differential equations would mean that, in these cases, we would also have to simulate idle pixels at smaller step sizes, even when it would be unnecessary. This would be a waste of computational power.

5 Results

The following simulations are all based on the pixel defined in Table 1. It is based on the Hybrid SPA pixel described by Smith et al. (2016). These SPA-pixels (Small Pixel Array) are part of a proposed sub-array of the X-IFU’s Large Pixel Array (LPA). They are designed to be placed in the center of the detector, meaning they would have the highest photon count rates during most observations. In order to still resolve single events, they thus require very small fall-times. Since the count rate should be highest for these pixels, they should also be among the ones most affected by crosstalk.

Both simulated pixels are assumed to have the same parameters aside from carrier frequency. Here, G is the heat conductance from absorber to the heat bath and TTR is the transformer turns ratio. Note that, as described in Section 3, my crosstalk calculations use the values for L_C and L_{filter} in this table down-transformed by TTR^{-2} . Voltage and current values are given as their equivalents in the TES-subcircuit. Since I wanted to analyze even very low crosstalk signals, I disabled the simulation of any noise. The weakest crosstalk events I simulate will turn out to be below noise level (see Sec. 5.2), such that they will not need to be considered in detector-level simulations. Further work will be necessary in order to qualify the events which fall below this threshold.

5.1 Operating Point Offset

The first basic crosstalk effect appears not only due to perturber pulses, but is rather a constant operating point offset in the signal pixel. This contribution comes from the constant additional Joule power due to the common impedance crosstalk from Eq. 21. Depending on the sign of $(\omega_2 - \omega_1)$, this constant offset may either be an increase ($\omega_1 > \omega_2$) or a decrease ($\omega_1 < \omega_2$) of the operating point temperature.

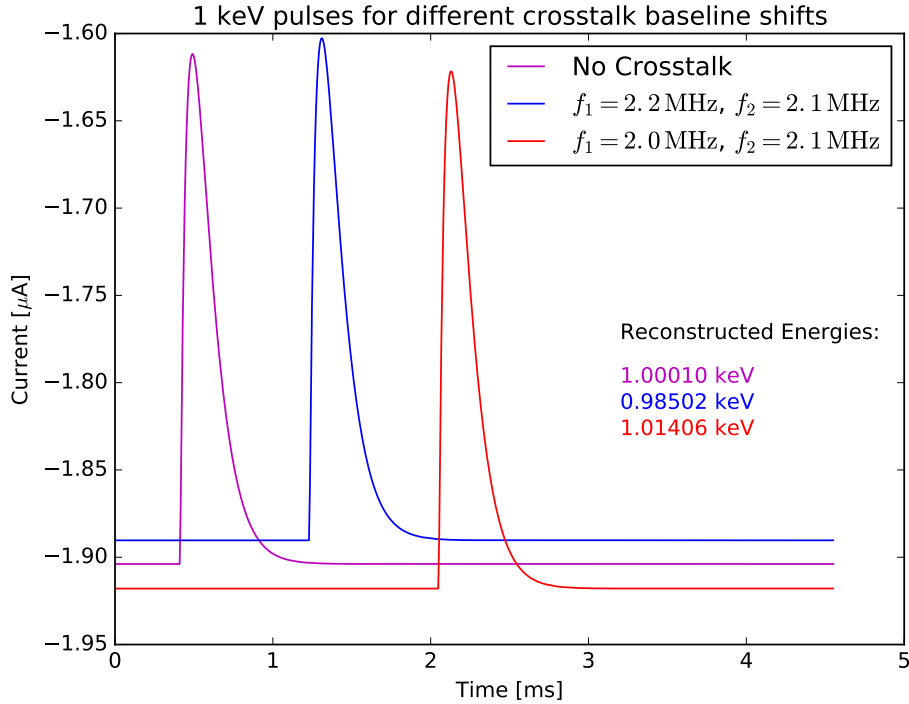


Figure 7: Effect of the shift in operating point due to constant common impedance crosstalk. I simulated 1 keV photons on the signal pixel, which is affected by the constant change in Joule heating due to common impedance crosstalk. The difference in reconstructed energies shows the calibration issues.

Figure 7 shows this shift in the operating point current, as well as the effect on the energy reconstruction. At different frequency combinations, I simulated a perturber pixel with no incident photon and a single 1 keV pulse on the signal photon. Since the signal pixel is in a different state for each simulation, it also reacts slightly differently to an incident photon of the same energy – the produced pulse shapes are slightly different. As such, the optimal filter which has only been calibrated for an unaffected pixel finds slightly different energies for each pulse. For this case, the variation in energy is of the order of 10 eV.

There is a caveat to this finding: In a realistic detector, the signal pixel would receive this constant crosstalk from more than one pixel. If the pixel has two neighbouring pixels with frequencies above and below the signal frequency, this effect should be partially canceled out, since the sign of the operating point offset is dependent on the frequency difference. However, Eq. 18 shows that this effect is not entirely symmetric in frequency space, such that there would still be a remaining offset. A simulation of more than two pixels would, as such, yield a more accurate estimate of this setpoint offset.

All in all, this effect poses a calibration issue; it will appear in a real detector and will have to be taken into account during its calibration. In order to accurately reconstruct these energies for *teslute*, one would have to calibrate the energy reconstruction individually for each frequency combination. This has, however, not been done for the following simulations.

5.2 Crosstalk Pulses

After understanding the constant effects of crosstalk, we can now examine the crosstalk signal for a perturber TES receiving photons. Figure 8 shows the crosstalk signal of 10 keV perturber photons for two different carrier frequency combinations. In order to study them separately, I have simulated both the total crosstalk as well as the individual carrier overlap and common impedance contributions. To

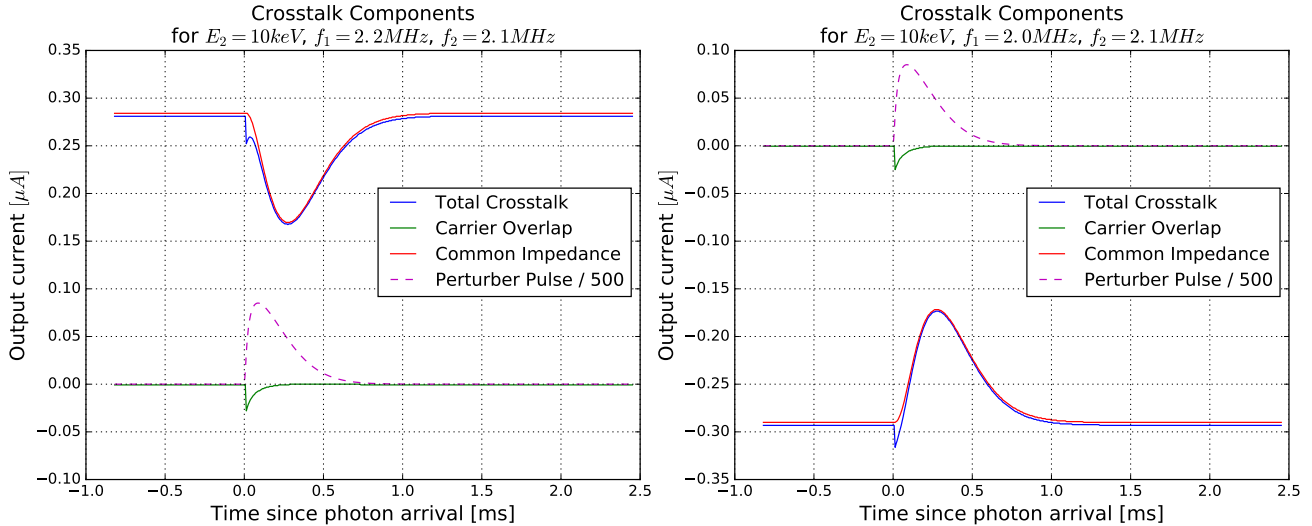


Figure 8: Individual crosstalk pulses simulated via `teslute`. For comparison, the downscaled perturber pulse has also been plotted. Depending on the frequency differences, the common impedance pulse may be positive or negative. Note that the common impedance pulse has a slower response time than the carrier overlap pulse, due to the former being an electrothermal effect.

compare their shapes, I have also plotted the perturber pulse, scaled down by a factor of 500.

The results of these plots are consistent with our earlier calculations: The signs of the common impedance pulses agree with the sign of $f_2 - f_1$. A common impedance pulse is always opposed to the offset due to the constant common impedance – this comes from the fact that the setpoint current is positive, while the heating due to incident photons causes a lower current in the perturbing TES. Note once again that the current output of `tessim` and `teslute` has been inverted and the baseline current has been subtracted.

The carrier overlap crosstalk pulses always have a negative sign, regardless of signal and perturber frequencies.

We can see that in the pixel simulated here the common impedance contribution dominates the crosstalk signal. It is also interesting to note that the carrier overlap pulse has a very similar rise time to the perturbing pulse, since they both directly originate from the change of resistance in the perturber pixel. The common impedance pulse has a longer rise-time due to its electrothermal nature – the increase in the perturbing current leads to additional Joule heating for as long as the perturbing current is below its set point. This behavior is opposed to a current pulse due to an incident photon, where all energy is dumped instantly.

For the effect of the crosstalk on the energy resolution in a realistic detector, it is also interesting to consider its magnitude compared to that of the intrinsic TES noise. In Figure 9, I have simulated a series of perturber photons with linearly increasing energies, where the simulation of noise in both pixels has either been enabled or disabled. The energies increase from 0.2 keV to 13.8 keV in steps of 0.4 keV.

One can see that the weakest pulses actually disappear entirely under the noise level, while higher energy pulses are clearly distinct from the noise. The peaks of the latter are, however, still strongly impacted by current fluctuations due to noise. In a power law spectrum, the photon flux at low energies is higher, such that most crosstalk events may also be below noise level. In general, the relative impacts of noise and crosstalk on energy resolution will depend on the precise spectra of the observed sources. Simulations of these realistic sources will be necessary in order to decide which effect is more critical and what design steps should be taken in order to improve resolution.

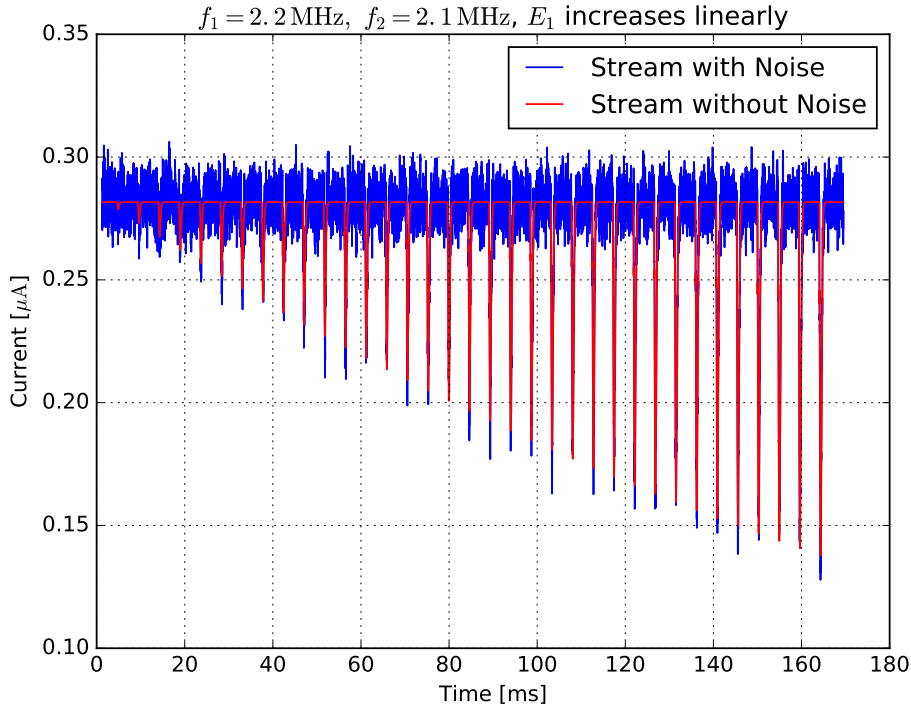


Figure 9: Two `teslute` runs with perturber energies increasing linearly from 0.2 to 13.8 keV in steps of 0.4 keV. The simulation of noise is either disabled or enabled. One can see that the smaller crosstalk pulses disappear under the noise level, while the peaks of the larger pulses are still strongly modified by noise.

5.3 Lookup Table

Simulating the entire X-IFU detector with roughly 4000 TES pixels separated into several readout chains (Barret et al., 2016) via an extension of `teslute` to a full array would be very inefficient, with simulations of single observations running much longer than the actually simulated exposure times. In order to do detector-level simulations, we instead use the `xifupipeline`, which linearizes the entire observation process, interpolating between energy values determined ahead of time with more precise simulation tools saved into so-called lookup tables.

The approach for the simulation of crosstalk events is quite the same (den Hartog et al., 2016) – when two photons arrive at two pixels in the same readout chain with time differences where those events may affect each other, we use a lookup table to compute the energy output of those pixels. The currently implemented format of the lookup table is three-dimensional – for a given energy of the perturber photon and the carrier frequencies of the signal and perturbing TES, it lists the energy deposited in the signal TES by crosstalk in eV. Additionally, we use time dependence weights, where the energy value in the lookup table is multiplied by an additional factor depending on the difference in arrival times between signal photon and perturber photon. The crosstalk energy interpolated from these tables is then simply added to the signal energy. I will also calculate a set of time dependence weights in Section 5.4.

Previous simulations (den Hartog et al., 2016) used a lookup table calculated outside of `tessim`, which assumes that the resistance of the signal TES stays constant during crosstalk events. The common impedance crosstalk, however, is entirely predicated on the change in the signal TES resistance due to a fluctuation in its Joule heating. Thus, I believe that `teslute` simulations should yield more accurate crosstalk values.

The generation method for a lookup table is fairly straightforward: For any combination of signal and

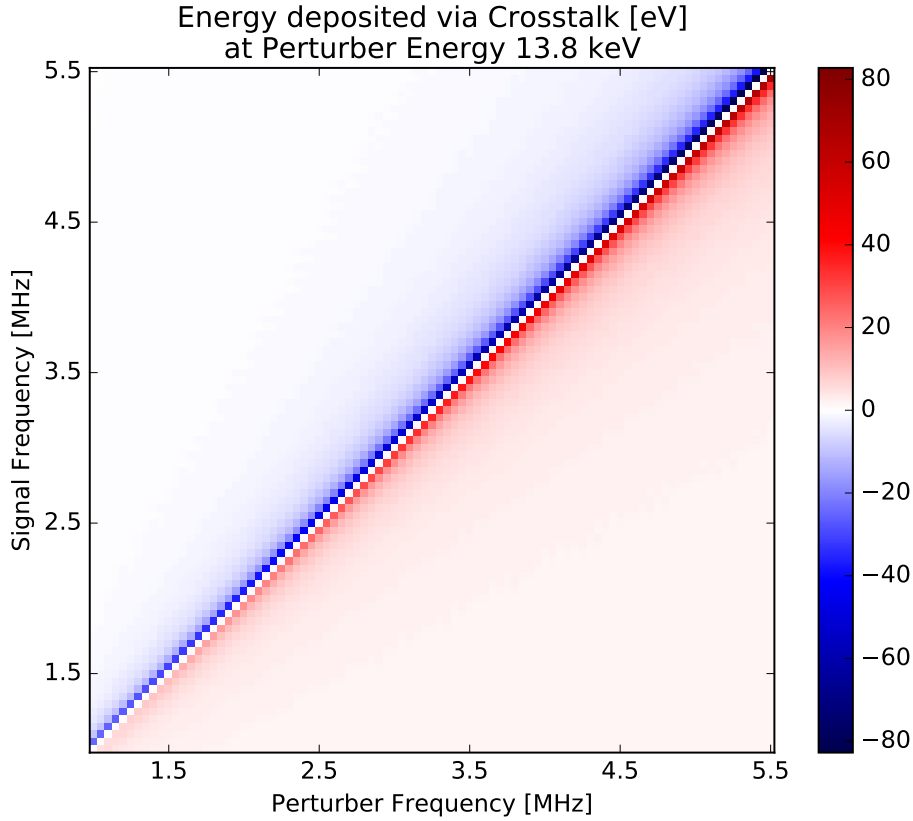


Figure 10: A slice of the lookup table generated via `teslute` at a constant perturber energy. Crosstalk is strongest along the sub- and superdiagonals, where the frequency differences are at their minimum. Its magnitude also increases with the perturber frequency.

perturber frequencies between 1 and 5.5 MHz in steps of 50 kHz, I simulated a series of photons with linearly increasing energies incident on the perturber pixel – the very same stream used to generate Fig. 9, in fact. The signal pixel received no photons in these simulations. The crosstalk pulses in the signal pixel were then triggered via my own impact-time based trigger. I then applied the optimal filtering reconstruction to those pulses and wrote the resulting energies into the lookup table.

Note that directly retrieving crosstalk energies from the pure crosstalk pulses is an idealization; in a real detector, those pulses should not be registered as actual events, as they should be below the triggering threshold – or even below the noise level (see Sec. 5.2). The realistic scenario would have photons incident on both the signal and perturbing TES, where we would measure the difference in the energies reconstructed from a signal pulse unaffected by crosstalk to a pulse affected by crosstalk. This would then take into account that the state of the signal pixel is also altered while it receives photons, instead of simply adding the energy reconstructed from a pure crosstalk pulse to that of an unaffected signal pulse.

Figure 10 shows a slice of the lookup table generated via `teslute`. In this plot, the dimension of the table has been reduced by choosing a constant perturber energy.

The crosstalk for equal signal and perturber frequencies has been defined as 0 eV. The color plot clearly shows that the crosstalk energy is positive for $f_2 > f_1$ and negative otherwise, since common impedance dominates all crosstalk. We can also see that the crosstalk is strongest along the sub- and superdiagonals, where frequency differences are at their lowest. As expected from Eq. 21, the common impedance crosstalk also becomes stronger with increasing perturber frequencies.

In order to offer a more detailed picture than a color plot, the left panel of Figure 11 shows a slice of Fig. 10 with a constant signal frequency. Here, the asymmetry of the simulated crosstalk becomes very

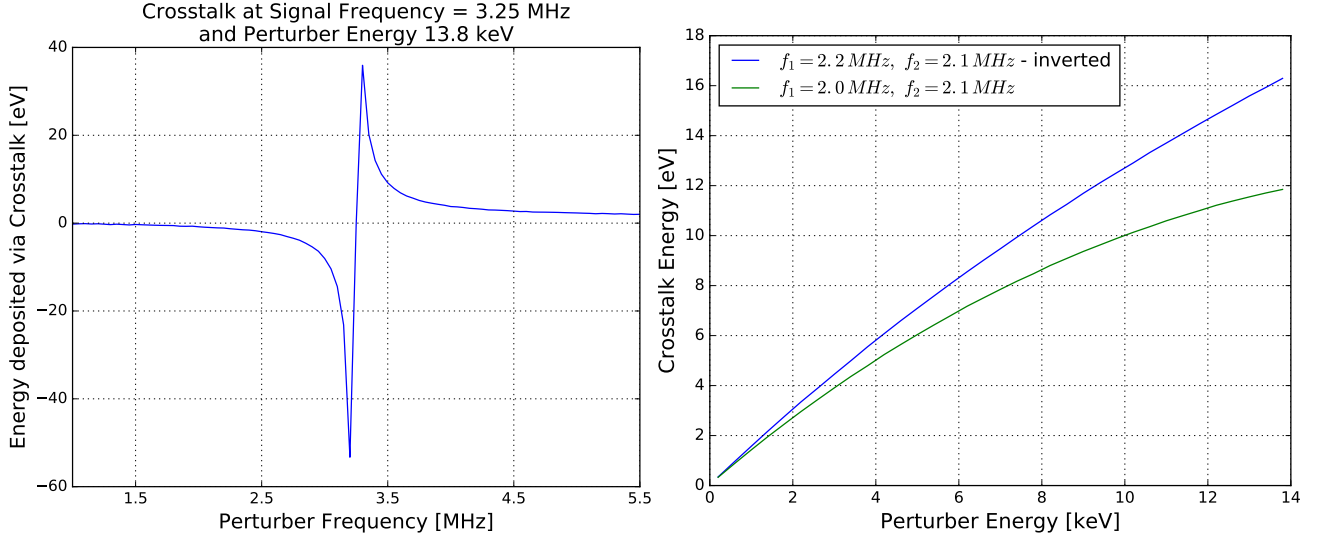


Figure 11: *Left*: Lookup table values for a constant signal frequency, showing the frequency asymmetries in crosstalk. *Right*: Lookup table values for constant frequencies and varying perturber energies – the crosstalk is non-linear in energy. Note that the crosstalk energies at $f_1 = 2.2$ MHz have been inverted.

clear. For one, at perturber frequencies close to the signal frequency, the negative crosstalk is slightly stronger than the positive crosstalk. This most likely comes from the carrier overlap crosstalk, which produces negative pulses, regardless of the sign of $f_2 - f_1$. Secondly, one can see that while the negative crosstalk goes down to close to 0 eV at high frequency distances, the positive crosstalk decays much more slowly, remaining slightly above 1 eV even at the maximum distance. This behavior is a result of the inherent asymmetry in common impedance crosstalk, as for these regions, the usual assumption that Z_{I,ω_2} is simply proportional to $(\omega_2 - \omega_1)^{-1}$ is no longer valid. By neglecting the contribution of R_2 in Eq. 22, the magnitude of the crosstalk power is rather proportional to $\frac{\omega_2^2}{\omega_2^2 - \omega_1^2}$. My more detailed simulations take the precise value of Z_{I,ω_2} into account. The right panel of Figure 11 shows the dependence of crosstalk on the perturber energy for two different frequency combinations, where the sign of the negative crosstalk has been inverted for the sake of comparison. This shows that the dependence of crosstalk on the perturber energy is non-linear. It also shows that at low frequency differences, the negative crosstalk is consistently stronger in magnitude than the positive crosstalk.

As an additional feature, I have also produced lookup tables for hypothetical detectors which only experience either carrier overlap or common impedance crosstalk. This scenario is generally unrealistic, since the common impedance crosstalk is essentially caused by carrier overlap crosstalk. The purpose of these tables is to be able to manually vary the magnitude of both types of crosstalk individually, in order to assist in detector design.

Note that the simulations of pure carrier overlap crosstalk use Eq. 12 with a value of $L_C = 0$, while the pure common impedance simulations assume that $I_{\text{readout}} = I_1^{\omega_1}$.

Figure 12 show the same plot as the left panel of Fig. 11 for both components. These plots nicely demonstrate two aspects of crosstalk: First, common impedance crosstalk is the dominant effect at all frequencies. Second, the carrier overlap crosstalk strongly contributes to the asymmetry of the total crosstalk at low frequency differences – at $\Delta f = 0$, the carrier overlap keeps the same sign, while the sign of the common impedance component switches.

Close to $\Delta f = 0$, the carrier overlap crosstalk also shows a much steeper decay than the common impedance crosstalk – the former falls down to ten percent of its maximum strength within 200 kHz,

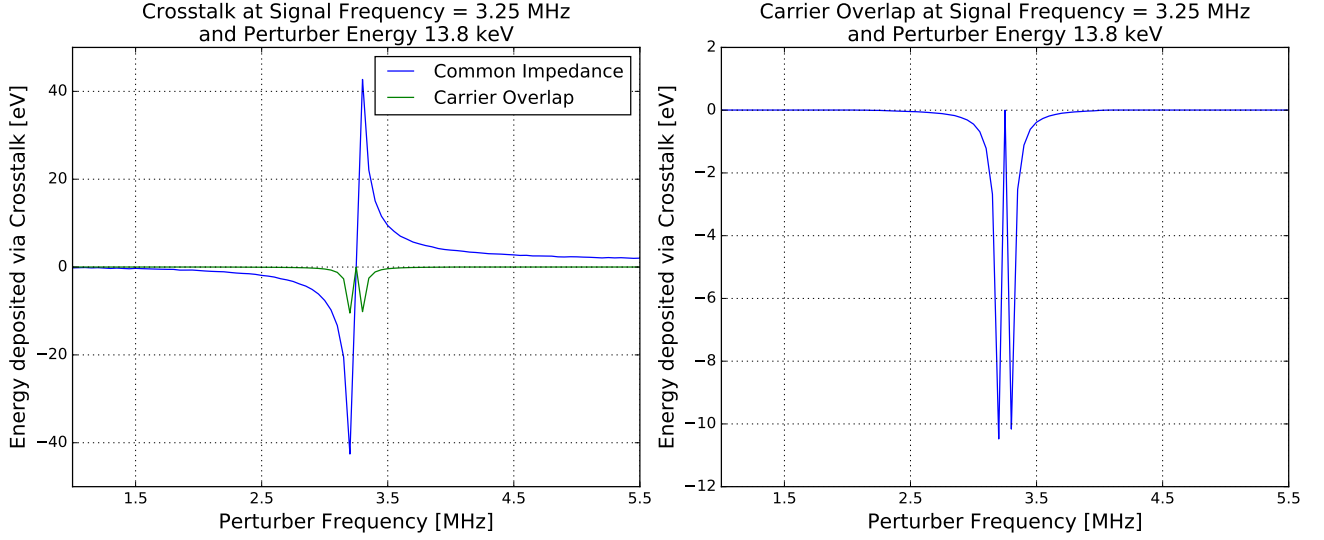


Figure 12: The same plot as the left panel of Fig. 11, but separated into carrier overlap and common impedance. *Left*: Both components in the same scale. The common impedance crosstalk dominates, while the carrier overlap crosstalk contributes an asymmetry at low frequency differences. *Right*: An individual plot of the carrier overlap values at a smaller scale.

while the latter stays above ten percent of its maximum strength within 500 kHz (The maximum crosstalk value recorded is for $\Delta f = 50$ kHz). Estimations from before align with these results – while the strength of carrier overlap is proportional to $(\Delta\omega)^{-2}$ (see Eq. 13), the common impedance crosstalk is proportional to $\frac{\omega_2^2}{\omega_2^2 - \omega_1^2} \approx (2(\omega_2 - \omega_1))^{-1}$, for low Δf .

5.4 Time Dependence

The lookup table in the previous section contains the reconstructed energies for pure crosstalk pulses which are perfectly triggered. This data alone is not yet sufficient for accurate predictions of the impact of crosstalk on the readout of a signal photon – one also has to take into account the difference in arrival times of the perturbing photon and the signal photon. For instance, a perturber photon arriving before a signal photon would change the state of the signal TES before it receives the second photon, affecting the pulse shape. A delayed perturber photon may instead cause a perturbation while the signal TES returns to its operating point, changing the pulse shape in a different way.

In order to understand these effects, I have run a series of simulations in `teslute`. For the signal pixel, I have generated a stream of photons at constant energies incident every 10 ms. For the perturbing TES, I have generated another stream of constant energy photons, where the photons arrive every 10.01 ms, starting slightly earlier than for the signal TES. As such, the first perturbing photon arrives 1 ms before the first signal photon, after which the difference in arrival time changes due to the different arrival rates. The difference in arrival time then goes linearly from -1 to 4 ms, where a negative sign implies the perturber photon arriving earlier.

For the so defined pixel impact lists, I have run several `teslute` simulations for different photon energies and frequency combinations. In the left panels of Figures 13 and 14, I am plotting the reconstructed energies of the simulated signal photons for either varying perturber frequency (Fig. 13) or perturber energy (Fig. 14). In order to better compare the shapes of these curves, the right panels contain the same datasets, where the energy reconstructed from an unaffected pulse has been subtracted from the reconstructed energies and the resulting values have been normalized to 1 for simultaneous perturber and signal impacts – i.e. at 0 ms delay. As such, one can obtain the energy by which the

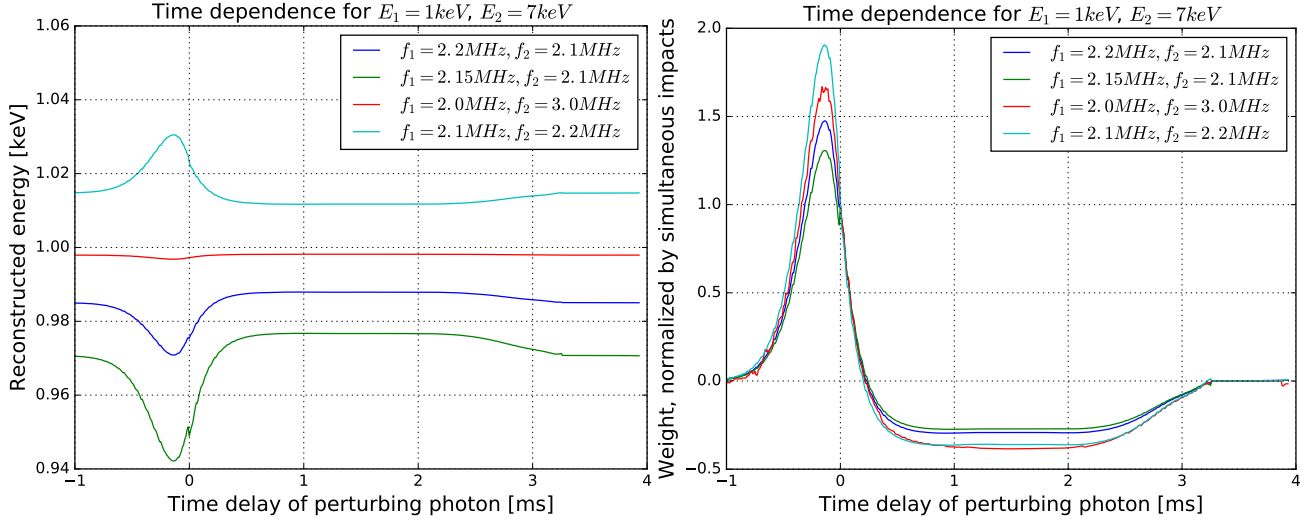


Figure 13: *Left*: Reconstructed energies of 1 keV signal pulses affected by 7 keV crosstalk pulses. The time delay of the perturber photon varies and we plot different frequency combinations. At around 3.3 ms, the crosstalk pulse no longer affects the signal pulse. *Right*: The same values, where the energy of the unaffected pulse has been subtracted and all curves have been normalized to 1 at 0 ms delay.

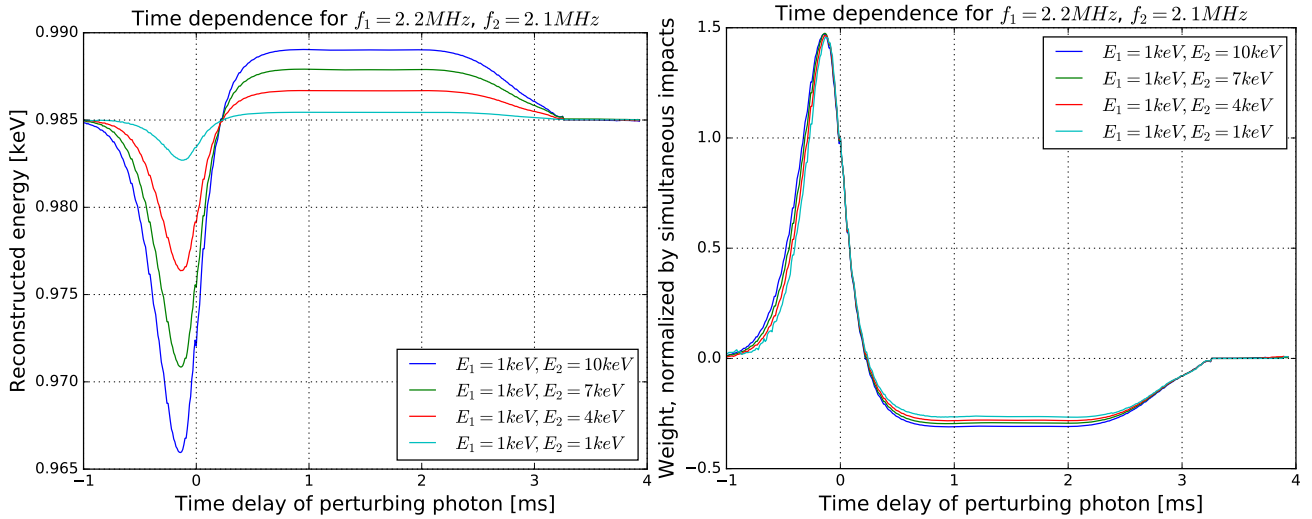


Figure 14: *Left*: Reconstructed energies of 1 keV signal pulses affected by crosstalk pulses of varying energies. The time delay of the perturber photon varies while the frequency combination is constant. At around 3.3 ms, the crosstalk pulse no longer affects the signal pulse. *Right*: The same values, where the energy of the unaffected pulse has been subtracted and all curves have been normalized to 1 at 0 ms delay.

signal pulse has been modified by multiplying the time dependence weights in these figures with the lookup table energy at the given frequency combination and perturber energy.

I have also run similar simulations for varying signal energies with constant perturber energies, whose results are displayed in Figure 15. Note that in the left panel, the energies reconstructed from unaffected signal pulses have already been subtracted so as to be able to plot all curves at the same scale. The right panel has been calculated in the same way as for Figures 13 and 14.

The time dependence curves all share some similar features: From a delay of about 3.3 ms on, the reconstructed energies stay constant. This comes from the length of the triggered records being 512 samples, which – using the sample times from Table 1 – corresponds to 3.28 ms. As such, those

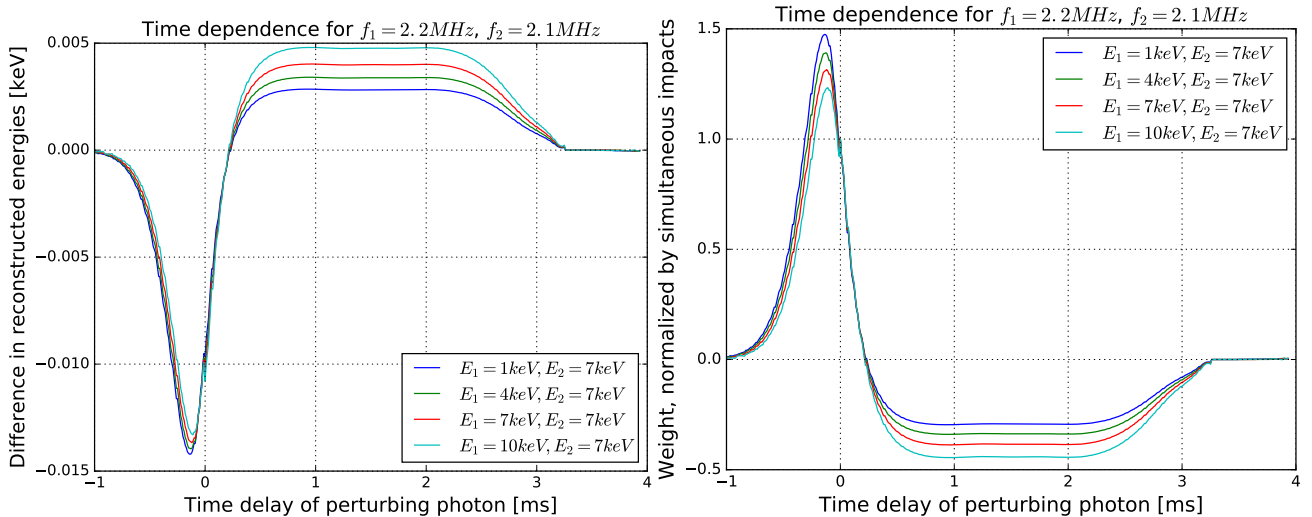


Figure 15: *Left*: Reconstructed energies of varying signal pulse energies with constant perturber energies. In order to plot them at the same scale, the energy of a signal pulse unaffected by crosstalk has been subtracted. The time delay of the perturber photon varies while the frequency combination is constant. At around 3.3 ms, the crosstalk pulse no longer affects the signal pulse. *Right*: The same values, where all curves have been normalized to 1 at 0 ms delay.

last photons are entirely unaffected by crosstalk, as the additional pulse is not even recorded. The differences in the energies reconstructed in Figure 13 at these delay times are purely due to the shift in operating point outlined in Section 5.1.

Another common feature is the fact that the crosstalk events with the strongest impact actually come from the perturber photons arriving slightly before the signal photon. This effect is not entirely unexpected – as shown in Section 5.2, the common impedance pulses – which are the dominant crosstalk mechanism in the pixels I’m considering – have a somewhat delayed rise time, taking about 0.2 ms to reach their peak. It makes sense, then, that the crosstalk events where this rise time is compensated by an earlier perturber pulse have the strongest impact. Time dependence tables from purely electrical simulations (den Hartog et al., 2016) peak at a delay of 0 ms, since they don’t incorporate this electrothermal effect.

The last feature worth pointing out is the long plateau of a suppressed and inverted crosstalk weights between delays of about 0.5 and 2.5 ms. This should entirely be a reconstruction effect, since the perturber photon arrives sufficiently later than the signal photon such that these pulses never directly interact. In the optimal filtering method, this region after the signal current pulse is weighted negatively, leading to this additional feature.

While the current implementation of the `xifupipeline` uses one set of time dependence weights for all crosstalk events, Figure 13 shows that this may be an incorrect estimation. One can clearly see in the right panel that the maximum weights differ by a factor of up to 50% at different frequency combinations. For different perturber energies, Figure 14 shows a much more consistent set of weights. Thus, I suspect that the different peak weights may come from the frequency asymmetries shown in Section 5.3 or the setpoint offset in Section 5.1. Whatever the cause may be, the mere presence of this inconsistency warrants future investigation, as well as an extension of the lookup table using different time dependence weights at different frequency combinations.

Figure 15 also shows a problem in the assumption of uniform time dependence weights – even for the same frequency combinations, the effect of crosstalk on a signal pulse is also dependent on the signal energy. This behavior is not surprising as such, since the state of the signal TES and its pulse shape (see Figure 3) vary dramatically. This also questions the validity of the current form of the lookup

table, since all values there have been reconstructed from pure crosstalk pulses and are then simply added to the energy of the signal pulses, no matter the signal energy.

All in all, these results indicate that extending the current lookup tables to also be dependent on the signal energy and with time dependence weights varying for different parameters would provide a significantly more accurate way of implementing crosstalk in the `xi fupipeline`.

6 Outlook and Conclusions

The results of this thesis are very promising but also warrant further investigation – I have successfully implemented the simulation of crosstalk into `tessim` and can produce lookup tables and time dependence values which can be used in the `xifupipeline`. We now also have the ability to extend our lookup table by taking into account the state of the signal pixel during a crosstalk event as well as the difference in timing effects for different scenarios.

As a preliminary result, crosstalk energies appear to be below a threshold of 100 eV for the simulated configurations (Fig. 10 is the worst case with the highest perturber energies simulated). There is also a certain degree of asymmetry for different frequency combinations. These results will assist in the design of the X-IFU detector.

However, there is still room for improvement: For instance, the effect of the constant common impedance (Sec. 5.1) will most likely differ when simulating more than one perturbing pixel, as these offsets may cancel each other out. Extending the simulation to a greater amount of pixels may yield a more accurate picture, although the simulation of large arrays will not be computationally viable.

Simulating small arrays of TES pixels will also open the possibility of comparing the output of my crosstalk model with experimental data from the FDM readout arrays currently being tested at SRON (Akamatsu et al., 2016).

Using my crosstalk simulator, one could now also perform simulations for more realistic sources. The photon streams I have generated up until now were from very artificial sources, since I directly wrote the impact files I needed for my measurements. With realistic sources, one could for instance study the degradation of the energy resolution due to crosstalk for different observation scenarios.

In line with such measurements, we can also compare the performance of the lookup table based approach of the `xifupipeline` with that of `tessim` and `teslute` – it is possible that for certain kinds of sources, the former approach may break down, requiring more accurate – and time-consuming – simulations.

7 Acknowledgments

I would like to thank Jörn Wilms and Thomas Dauser for their supervision during my work for this thesis, as well as Roland den Hartog and Steven Smith for their information regarding the design of TES pixels and readout techniques. `teslute` was developed based on TES simulator code written by Steven and Jörn; the entire SIXTE package was developed by too many people to list here. The optimal filtering files used in my energy reconstruction were provided by Philippe Peille, who also helped me with their application and provided general advice for my simulations.

In general, I'd like to thank all of the participating scientists of the Athena end-to-end simulations as well as the members of the Dr. Karl Remeis-Observatory, who have made this project a very pleasant and rewarding experience for me.

List of Figures

1	<i>R(T)</i> -curve for a transition-edge sensor	4
2	Principle of <code>tessim</code> and <code>xi</code> pipeline.	5
3	Examples of pulses produced by <code>tessim</code>	7
4	Circuit diagram for the FDM-readout scheme.	8
5	Simplified circuit diagram corresponding to Fig. 4.	9
6	Working principle of <code>teslute</code>	12
7	Effect of the shift in operating point due to constant common impedance crosstalk.	14
8	Individual crosstalk pulses simulated via <code>teslute</code>	15
9	Comparison of the noise level with crosstalk pulses.	16
10	A slice of the lookup table generated via <code>teslute</code> at a constant perturber energy.	17
11	Lookup table values for different parameters set to be constant	18
12	Separated lookup table values for individual crosstalk effects.	19
13	Time dependence for varying frequency combinations	20
14	Time dependence for varying perturber energies	20
15	Time dependence for varying signal energies	21

List of Tables

1	Physical parameters of the TES-pixels simulated in this thesis.	13
---	---	----

References

- Akamatsu H., Gottardi L., van der Kuur J., et al., 2016, Development of frequency domain multiplexing for the X-ray Integral Field unit (X-IFU) on the Athena
- Andrews D.H., Brucksch W.F., Ziegler W.T., Blanchard E.R., 1942, Review of Scientific Instruments 13
- Andrews D.H., Fowler R.D., Williams M.C., 1949, Phys. Rev. 76, 154
- Barret D., Lam Trong T., den Herder J.W., et al., 2016, The Athena X-ray Integral Field Unit (X-IFU)
- den Hartog R., Barret D., Gottardi L., et al., 2014, Requirements for the detectors and read-out of ATHENA X-IFU
- den Hartog R., Peille P., Dauser T., et al., 2016, The impact of crosstalk in the X-IFU instrument on Athena science cases
- Dobbs M.A., Lueker M., Aird K.A., et al., 2012, Review of Scientific Instruments 83
- Hitomi Collaboration, Aharonian F., Akamatsu H., et al., 2016, Nature 535, 117
- Irwin K., Hilton G., 2005, Transition-Edge Sensors, p.63, Springer Berlin Heidelberg, Berlin, Heidelberg
- Iyomoto N., Bandler S.R., Brekosky R.P., et al., 2008, Journal of Low Temperature Physics 151, 506
- Kinnunen K., 2011

- McCammon D., 2005, Thermal Equilibrium Calorimeters - An Introduction, p. 1
- Nandra K., Barret D., Barcons X., et al., 2013, ArXiv e-prints
- Peille P., Ceballos M.T., Cobo B., et al., 2016, Performance assessment of different pulse reconstruction algorithms for the ATHENA X-ray Integral Field Unit
- Rey C., 1991, Thermochimica Acta 184, 329
- Smith S.J., Adams J.S., Bandler S.R., et al., 2016, Transition-edge sensor pixel parameter design of the microcalorimeter array for the x-ray integral field unit on Athena
- Wang T.S., Guo G.C., Zhu Q.F., et al., 2012, IEEE Transactions on Applied Superconductivity 22, 2100212
- Wilms J., Brand T., Barret D., et al., 2014, ATHENA end-to-end simulations
- Wilms J., Smith S.J., Peille P., et al., 2016, TESSIM: a simulator for the Athena-X-IFU

Erklärung

Hiermit bestätige ich, dass ich diese Arbeit selbstständig und nur unter Verwendung der angegebenen Hilfsmittel angefertigt habe.

Ort, Datum

Christian Kirsch